We are IntechOpen, the world's leading publisher of Open Access books Built by scientists, for scientists

4,800
Open access books available

122,000
International authors and editors

135M
Downloads

Our authors are among the

154
Countries delivered to

TOP 1%
most cited scientists

12.2%
Contributors from top 500 universities

WEB OF SCIENCE™

Selection of our books indexed in the Book Citation Index in Web of Science™ Core Collection (BKCI)

Interested in publishing with us?
Contact book.department@intechopen.com

Numbers displayed above are based on latest data collected.
For more information visit www.intechopen.com

23

Heat Absorption, Transport and Phase Transformation in Noble Metals Excited by Femtosecond Laser Pulses

Wai-Lun Chan[1] and Robert S. Averback[2]
[1]*University of Texas at Austin, Texas 78712,*
[2]*University of Illinois at Urbana-Champaign, Illinois 61801, USA*

1. Introduction

With the rapid development of short pulse lasers, femtosecond (fs) lasers have been used in technologies such as materials modification (Vorobyev & Guo, 2008), micromachining (Liu et al., 1997; Gattass & Mazur, 2008), and surface patterning (Miyaji & Miyazaki, 2008). However, details on energy absorption, heat dissipation, and phase transformation during the initial excitation of these intense pulses are poorly understood, despite their importance in determining the final microstructure and morphology of the laser-processed materials. Scientifically, intense laser pulses drive materials into highly non-equilibrium states, which provide us new opportunities in studying the fundamental properties of these states. By carefully controlling the relaxation of the excited materials, it is also possible to create novel metastable structures.

Before we can achieve these goals, we need a detailed knowledge on how materials respond to these intense pulses. This is a non-trivial task since the optical, thermodynamics and transport properties can change drastically upon intense laser irradiation. In this chapter, we summarize our recent works on Ag to illustrate some of the complexities involved in both heat transport and absorption at laser fluencies near the melting and ablation threshold. We observe significant heat confinement and absorption enhancement at high laser fluences. These differences derive mainly from the excitation of d-band electrons at high electron temperatures, which significantly changes the electronic properties, although many of the details remain poorly understood. From a more applied consideration, we show that by using fs-pulses, we are able to confine melting and ablation to the very top layers of the materials, which has important implications for pulsed laser deposition of ultra-thin layers and micromachining. Furthermore, we demonstrate that by utilizing the ultrafast quenching of the surface layer after laser excitations, we can create a pure metallic liquid at a temperature as low as 0.6 T_m, where T_m is the melting temperature of the metal. This degree of undercooling has not been achieved by other experimental techniques in pure metals and the transformation kinetics of this far-from-equilibrium state is not well-understood. Indeed, our results show that classical solidification theories cannot explain the experimental results and new atomistic mechanisms are needed in order to explain the measured kinetics.

2. Non-linear heating by a single laser pulse

Before we discuss the heat transport and phase transformation in noble metals irradiated by fs-lasers, we first need to consider how heat is absorbed by the materials during a single pulse irradiation. This is not a simple problem because, for a high intensity pulse with a finite width, the electrons excited by the early part of the pulse can alter significantly the reflectance during the latter part of the pulse. This integral effect makes the total absorbed energy depends not only on the transient reflectivity of the materials, but also on the pulse duration and the laser fluence. There are numerous time-resolved measurements on reflectivity changes in metals induced by fs-laser (see e.g. Norris et al., 2003; Eesley, 1983; Tas & Maris, 1994), but most of these studies are performed at relatively low excitations. Absorption measurements have been done at very high fluencies for studying the dynamics of electrons in the plasma state (Milchberg et al., 1988; Cerchez et al., 2008) and the energy that resides in the sample after laser ablation (Vorobyev & Guo, 2004). However, at a more moderate excitation, where processes such as melting and desorption occur, the change in absorption can still be significant, but they are often neglected. In the following, we summarize our absorption measurements in noble metals and show that excitation of d-band electrons significantly changes the optical properties of the materials, and therefore, the total energy absorbed. Knowing the actual amount of energy that is absorbed by the materials is important, for example, in determining how much materials can be melted by a single laser pulse.

2.1 Heat absorption measured by calorimetry

Instead of measuring the transient optical properties of the metals, we choose to measure the energy absorbed by the samples directly, using calorimetry method. A laser pulse with a wavelength of 800 nm and FWHM pulse duration of 140 fs was used to excite the sample. The same laser system was used for experiments described in the remainder of this chapter. The samples were 400 nm-thick metal thin films sputter deposited on a Si substrate. We thermally isolated the sample from the surrounding by holding the sample with a very fine (0.001") thermocouple wire. This allows us to measure the temperature change of the sample induced by the laser pulses before the heat is dissipated to the surrounding. Figure 1(a) shows a schematic of the setup. The absorption coefficient $A(f)$, defined as the absorbed energy divided by the incident energy, can be determined analytically by measuring the temperature change as a function of time. The detailed analysis can be found in (Chan et al., 2009a). Here, we discuss only our main results.

Figure 1(b) shows the $A(f)$ as a function of incident energy (solid square) for Ag. For comparison, the peak fluence f of the pulses is shown on the top axis. At low fluences, the measured $A(f)$ agrees well with the optical absorption calculated using the dielectric constant of Ag, which is ≈ 0.014. However, at higher incident energies, $A(f)$ deviates significantly from this theoretical absorption. Furthermore, since the measured $A(f)$ represents the *average* absorption coefficient over the entire Gaussian beam. Spatially, at the center of the laser beam, the fluence is much higher. Therefore, the actual absorption coefficient $a(f)$ at the center of the pulse can be much more sensitive to the change in the fluence as compared to $A(f)$. Mathematically, the actual $a(f)$ can be related to the measured $A(f)$ by:

$$A(f) f 2\pi\sigma^2 = \int_0^\infty a\left[f \exp\left(-\frac{r^2}{2\sigma^2} \right) \right] f \exp\left(-\frac{r^2}{2\sigma^2} \right) 2\pi r dr \,, \tag{1}$$

where r is the radial distance from the center of the pulse. For a Gaussian beam profile, $a(f)$ can be solved analytically (Chan et al., 2009b) and the calculated $a(f)$ is shown as the solid line in Fig. 1(b). We note that near the melting threshold (~ 0.4 J cm^{-2}), the actual absorbed energy can be 4 times as high as the absorption predicted by the optical constants of Ag.

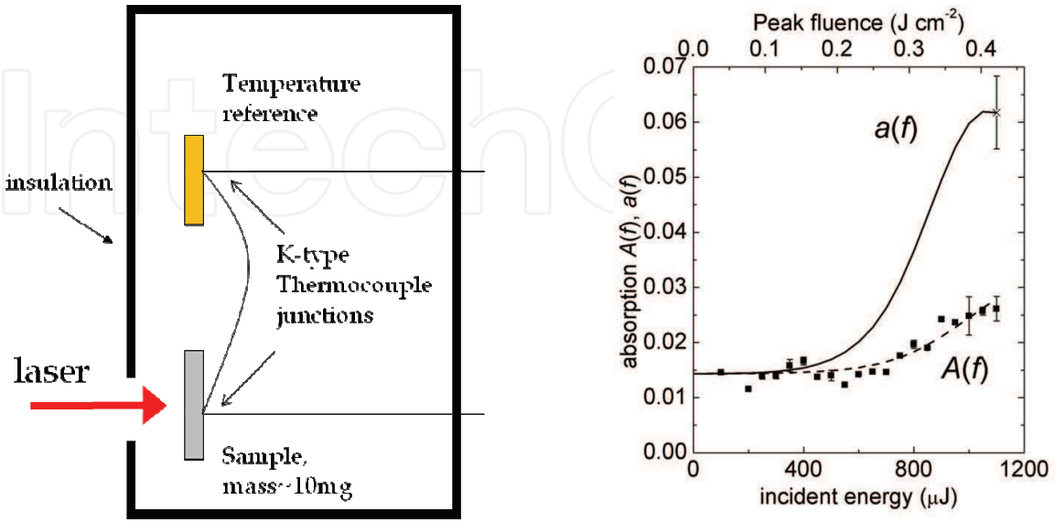

(a) (b)

Fig. 1. (a) Schematics of the calorimetry setup. (b) The absorption coefficient as a function of laser incident energy in Ag. (Figure reprinted from Chan et al., 2009a)

2.2 Physical origin of the increase in absorption

In noble metals, the optical properties in the visible range can be described by the Drude model of free electrons (Pines, 1999). In this model, the reflectivity depends on the electron scattering rate, which decreases with an increase in the scattering rate. The abrupt increase in the optical absorption in Fig. 1(b) can be explained by a sudden increase in the electron scattering rate. Using the band structure of Ag (Fuster et al., 1990) and assuming the electrons maintain a Fermi-Dirac distribution, it can be shown that the fluence where the absorption begins to increase corresponds to the excitation of the d-band electrons. Furthermore, we note that the conducting s-electrons are scattered far more strongly by d-band holes compared to other s-electrons. Indeed, the s-d electron scattering rate is ≈ 2 orders of magnitudes higher than the s-s electron scattering rate (Mott, 1936; Baber, 1937). As the d-holes are created, therefore, the electron-scattering time shortens significantly. This results in an abrupt increase in the energy absorption, as observed in our calorimetry experiment.

According to the above picture, there should not be a comparable increase in the absorption in noble metals that already have a significant number of d-band holes at room temperature. To create such a sample, for instance, we can dope Ag with transition metals to create "doped"d-band holes (Coles & Taylor, 1962). We conduct absorption experiments on dilute Ag alloys doped with a few atomic percent of Pt. The results are shown in Fig. 2. The absorption coefficient $a(f)$ is determined from the experimentally measured $A(f)$ using Eq. (1). To provide a direct comparsion of the laser-induced d-band holes and the doped d-band holes, we plot $a(f)$ as a function of absorbed fluence. The population of the excited d-band holes (for Ag) can be estimated for a given absorbed fluence by assuming the electrons maintain a Fermi-Dirac distribution. They are shown as verticle lines in Fig. 2.

At low Pt concentrations, the laser-induced d-band holes seem to be equivalent to the d-band holes produced by alloying. As shown by the dotted line, the absorption at low fluences of the 2.7 % alloy is similar to the absorption of Ag at an absorbed fluence that can create ≈ 3% d-band holes. This particularly good agreement is probably somewhat fortuitous, considering that the laser-induced d-band holes are not physically the same as doped holes even though their effects can be similar. In addition, the calculated number of laser-induced d-band holes is the number of holes after the entire pulse is absorbed; the number of holes within the pulse duration will probably be less. Nevertheless, Fig. 2 suggests that the nature of the two kinds of holes is similar. For the fluence dependence, similar to Ag, the 2.7% alloy shows an increase in absorption at higher fluences. For the 8% alloy, we do not see a measurable increase in absorption. This simply illustrates that for a sample that already has a significant number of d-band holes, the laser fluence has little effect on increasing the overall optical absorption.

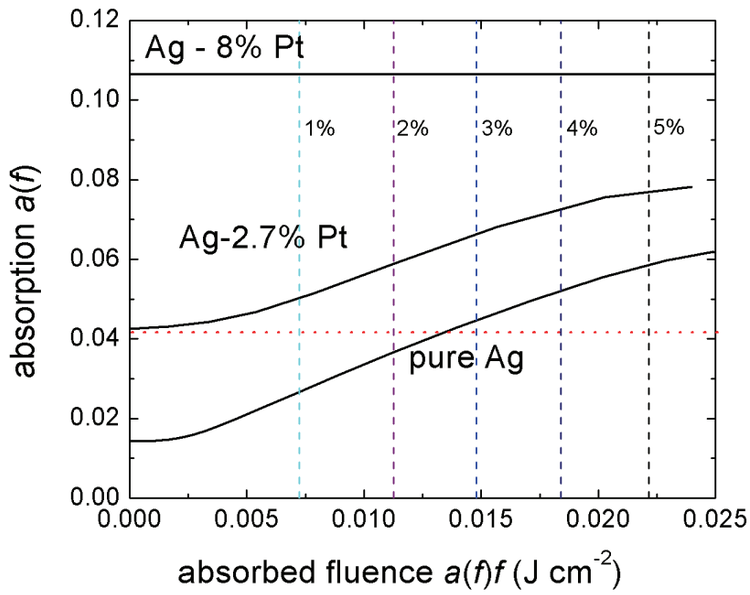

Fig. 2. Optical absorption as a function of absorbed fluence for diluted Ag alloys. The vertical lines represent the calculated population of laser-induced d-band holes. (Figure reprinted from Chan et al., 2009a)

From the above measurements, we can see that the optical absorption can vary significantly with the laser fluence. This is because electron bands under the Fermi-level, which normally remain filled at low excitations, can be excited at higher laser fluences. This significantly changes the optical response of the materials. We have qualitatively explained this absorption change by d-band excitation in Ag. Unfortunately, formulating a more quantitative model is challenging, even for simple materials such as noble metals. This is because our understanding on electron properties at these high excitations is limited.

3. Ultrafast melting in silver

The strong excitation of electrons not only changes the optical properties of the materials, but also the transport properties. The transport properties of these excited electrons

determine how heat is dissipated from the initially excited region. This in turn controls how much materials is heated up and, in some cases, transformed to a different phase in the regions within and beyond the excitation depth of the laser. Technologically, fs-lasers are believed to be better tools for laser-machining and materials modification compared to ps- or ns-lasers. This is because the faster heating of fs lasers results in a better heat confinement near the surface region. In the other words, it creates less damage to materials beyond the optical absorption depth of the laser. Understanding the heat deposition profile after fs-laser irradiation is critical to these applications. However, the heat dissipation mechanisms are difficult to measure and still poorly understood.

In this section, we present our recent measurements on the melting dynamics of Ag. We measure the melt-depth as a function of time. The melting dynamics cannot be explained by the well-known transport properties of noble metals. More specifically, the melt-region is much shallower than what is predicted by the hot electron transport properties of Ag. Additional heat confining mechanisms are needed to explain the observed dynamics. As we have mentioned, the d-band electrons, even though they are ≈ 3 eV below the Fermi level in Ag, can be excited at high fluences. They affect the electron transport properties and the observed melting dynamics.

3.1 Measurements on the propagation of the melt-front into a superheated solid

To measure the depth of melt as a function of time after laser excitation, we performed time-resolved optical third harmonic (TH) generation measurements. Optical TH generation is extinct in an isotropic phase (e.g. liquid) but usually not in a crystalline phase (Butcher & Cotter, 1990). This gives us large measurement contrast between the two phases. The experimental details and the calibration methods can be found in (Chan et al., 2008). Here, we will briefly summarize the experimental method.

All the measurements were done on single crystal Ag (001) grown on MgO substrates. Optical pump-probe experiment was done to determine the melt-depth as a function of time. A pump pulse was first used to excite the solid and a time-delayed probe beam with a beam diameter 10 times smaller than the pump pulse was used to determine the melt-depth at the center of the pump pulse. The intensity of TH generation from the sample surface, which induced by the probe pulse, was measured using a sensitive CCD camera. Ultra-fast melting usually creates a continuous liquid layer on top of the solid phase. Since the liquid phase does not generate TH light, the depth of the melt $d(t)$ can be related to the normalized intensity I through the exponential relationship:

$$I(t) = \exp\left[- d(t)\left(\frac{3}{d_I} + \frac{1}{d_{III}} \right) \right] \tag{2}$$

where d_I and d_{III} are the extinction depths of the fundamental and TH light. The 3 in the exponential term arises from the cubic dependence of the TH signal on the probe laser intensity. Equation (2) neglects the difference in the dielectric constant between the liquid and solid phase. This, however, is a good approximation for metals such as Ag, for which the two phases have a very similar dielectric constants (Miller, 1969). The combined extinction depth $(3/d_I+1/d_{III})^{-1}$ for high laser fluences is not known *apriori*, but we measured it separately in our control experiment with multilayer films with known thicknesses.

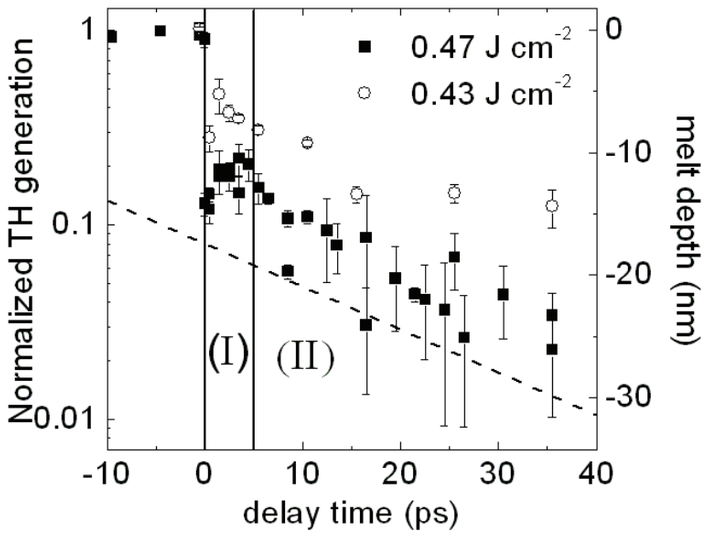

Fig. 3. Normalized TH generation as a function of delay time for a 200 nm Ag film. The axis on the right shows the corresponding melt depth. The melting can be divided into two stages: (I) initial melting due to transfer of energy from electron to phonon; (II) propagation of the melting front into the superheat solid. The dotted line represents a melting speed of 350 m s^{-1}. (Figure reprinted from Chan et al., 2008)

Figure 3 plots the melt-depth as a function of time at two different pump fluences. The data are plotted on a semi-log scale. According to Eq. (2), the slopes of the curves represent the velocities of the melt-crystal interface. The calculated melt-depth is shown on the axis on the right. The melting can be roughly divided into two stages. In the first stage, rapid melting occurs within first 5 ps. This corresponds to the electron-phonon coupling time in Ag (Ernstorfer et al., 2007; Lin et al., 2008b); i.e. time needed for the excited electrons to transfer the energy to the cold lattice. Following the initial fast melting, the melt-front propagates steadily into the bulk at a velocity ≈ 350 m s^{-1} (the slope for this velocity is shown as the dashed line in Fig. 3) for another 25 ps. The combined maximum melt-depth for both stages is ≈ 25-30 nm, which occurs at t ≈ 30 ps. Then, the melt resolidifed with much slower dynamics (the solidifcation kinetics will be addressed in Sec. 4).

A more surprising result is the melt-depth as a function of laser fluences for experiments performed on Ag films with different thicknesses. The results are shown in Fig. 4. We note that non-equilibrium electrons excited by the laser can carry heat away from the optical extinction depth before they couple to the phonons. This measurement characterizes the dynamics of these 'hot' electrons. Similar ideas have been used in (Suarez et al., 1995; Bonn et al. 2000) to study the fast electron transport at lower fluences. For the results represented in Fig. 4, we fix the delay time at 25 ps (onset before resolidification occurs) and measure the TH intensity as a function of pump fluence. The film does not melt until a threshold is reached. The amount of melt then increases approximately linearly with respect to the additional fluence. The threshold for melting and the amount of melt remains nearly independent of film thickness, until the thickness falls below 100 nm. Since heat transport across the Ag-MgO interface is negligible in 25 ps, the melting threshold should start to decrease when the film thickness falls below the depth of heat deposition. Therefore, the result indicates that at t = 25 ps, most of the heat is confined within the top 50 - 100 nm of the Ag.

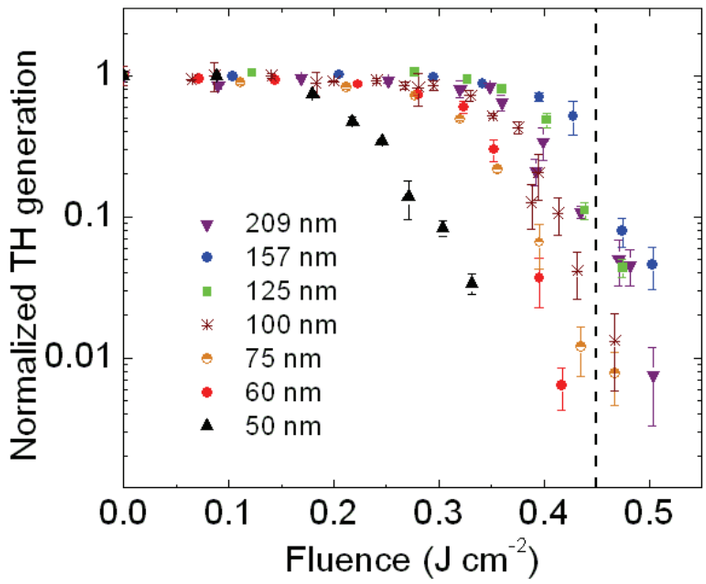

Fig. 4. TH generation as a function of pump fluence for different film thicknesses. The delay time is fixed at 25 ps. (Figure reprinted from Chan et al., 2008)

Experiments performed at lower fluencies (where d-band electrons are not excited) have indicated that hot electrons can carry heat a few times deeper than what we observe here via the so-call ballistic transport (Suarez et al., 1995; Bonn et al. 2000). Therefore, when the fluence is high enough to induce melting, the electron transport must change significantly to produce the heat confinment observed in Fig. 4.

3.2 Heat transport mechanisms

In order to understand what aspects of the heat transport can create the spatial confinement following, we use a two temperature model (TTM) to model the thickness dependences observed in Fig. 4. TTM (Anisimov et al., 1974) is a standard technique to model the evolution of electron and phonon temperatures. The details of our TTM can be found in (Chan et al., 2008) and will not be discussed here. Note that the model is not aimed at being rigorous for the first few ps after the excitations since such a treatment on the electron transport with d-band excitation that includes the consideration of non-equilibrium electrons, is beyond the scope of this chapter. The model described here is used to estimate the amount of heat confinement induced by excited d-band holes and to explore possible heat confining mechanisms.

It has been reported in other studies that the excitation of d-band electrons changes the electron heat capacity and electron-phonon coupling constant by an order of magnitude at high electron temperatures (Lin et al., 2008b). First, we include these effects into our TTM, but do not account for the effects of d-band excitation on electron transports. This result is shown as solid-squares in Fig. 5, which plots the maximum melt-depth as a function of film thickness at a given laser fluence. The experimental results are shown as solid-circles for comparison. We see that this model highly underestimates the melt-depth in the thick films. It also predicts that the melt-depth decreases significantly with an increase in film thickness. This contradicts to the experiment in which the melt-depth does not change significantly for

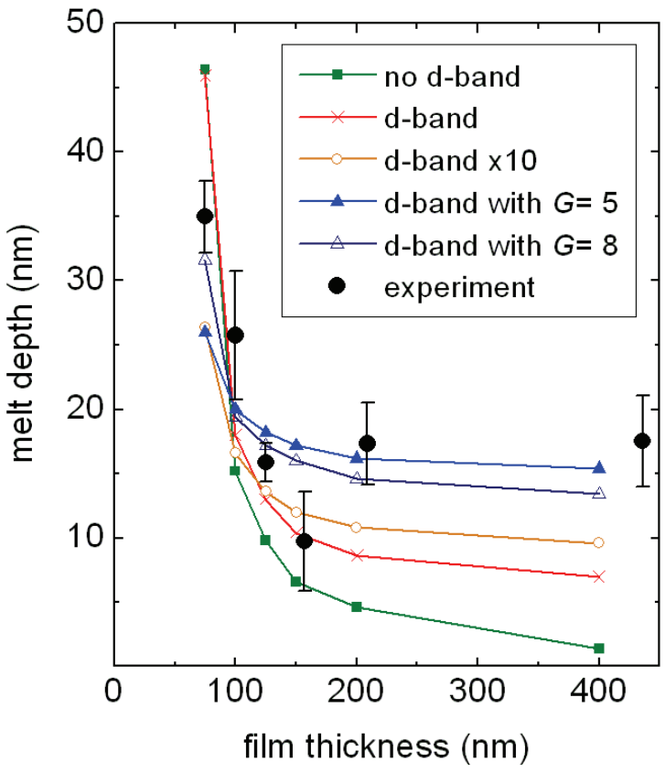

Fig. 5. Melt-depth as a function of film thickness at delay time equals to 25 ps. The experimental points (black-circles) are determined from Fig. 4, at fluence = 0.45 J cm^{-2} (the vertical dashed line in Fig. 4). For the TTM calculation, the absorbed fluence is fixed at 0.025 J cm^{-2}. The modeling parameters used are: green-line with squares – no enhancement in e-e scattering rate from d-band holes [C = 0 in Eq. (3)]; red-line with crosses – enhancement in e-e scattering modeled by Eq. (3), with C = 150; orange-line with open circles – C = 1500; blue-lines with triangles – C = 150, with the addition of an effective interface impedance G (see the text). Only G = 5 and 8 GW m^{-2} K^{-1} are shown. (Figure reprinted from Chan et al., 2008)

film thickness larger than 100 nm. This discrepancy is caused by neglecting the d-band excitation on thermal transport, which causes significant heat confinement. The overestimated heat conductivity allows heat to dissipate quickly from the surface region to the deeper region of the film, which reduces the overall melt-depth.

In Sec. 2, we have mentioned that the presence of d-band holes can increase the electron scattering rate. To account for the effect of d-band holes on electron scattering, we add the contribution of s-d scattering to the total scattering rate by the following phenomenological relationship:

$$A_{ee} = A_{ee,0}\left[1 + CN_h(T_{el})\right]. \tag{3}$$

In this equation, $A_{ee,0}$ is the e-e scattering coefficient in the low temperature limit, which for Ag is 0.13 m MW^{-1} (MacDonald & Geldart, 1980). N_h is the number of d-band holes per atom, which is determined by integrating the Fermi distribution. The constant C represents the ratio of the s-d electron scattering rate to the s-s electron scattering rate; we roughly estimate that C = 150, based on A_{ee} being about 2 orders of magnitudes larger in Ni than in

Ag (Mott, 1936; Baber, 1937). The TTM result with the inclusion of this reduced electron conductivity is shown as crosses in Fig. 5. Although the new results agree much better with the experiments, it still underestimates the melt-depth at larger film thicknesses. Increasing the constant C by another order of magnitude (open-circle) does not significantly change the result. An additional heat confinement mechanism is needed to explain the experimental data.

We explore possible additional mechanisms that can create the heat confinement necessary to explain the experimental results using the TTM; we do this by adding a thermal interface impedance. This is rationalized by recognition of the sharp interface that is created by the d-band excitations in the surface region. Since a large temperature gradient exists over a distance that is small compared to the electron mean free path, λ, of Ag [e.g. $\lambda \approx 50$ nm at RT (Kittle, 2005)], electron conductance on the 'cold' side of the interface can be overestimated in the above TTM. In other words, the excited d-band electrons should have influence on κ_{el} in the un-excited region, extending to a distance on the order of λ. A similar argument for non-local heat transport has been employed previously in (Mahan & Claro, 1988) to describe the reduction in phonon conductivity when the curvature in the temperature depth profile is large. We place the interface at a depth of 20 nm and assume its conductance varies inversely with the number of d-band holes. Since the number of d-band holes increases approximately linearly with electron temperature T_e above some critical temperature (≈ 4000 K), we take the interface conductance as $10000 \times G/(T_s\text{-}4000)$, where T_s is the surface temperature and G is a fitting constant with the unit of interface conductance. In the first 3-4 ps, T_s falls from around 15,000 K to a temperature below 4,000 K. Therefore, the interface is only active during stage I, shown in Fig. 3. We vary G from 2 to 12 GW m^{-2} K^{-1}. The melt-depth as a function of film thickness is shown in Fig. 5 (blue-lines with triangles). The prediction of the model agrees well with the experiment for $G \approx 5 - 8$ GW m^{-2} K^{-1}. For comparison, we note that the conductance of Cu-Al interface is 4 GW m^{-2} K^{-1} (Gundrum et al., 2005), and a conductance of 8 GW m^{-2} K^{-1} effectively reduces electron conductivity in a 50 nm-thick region in Ag by half. Therefore, the scattering of the conducting electrons by the d-band holes explains the heat confinement observed in experiments.

3.3 Melting dynamics and its implications

After the cooling down of the excited d-band holes (the end of stage I), the surface region is highly superheated. The melt-front continues to travel into the superheated solid but at the same time, heat is lost to deeper regions and the melting eventually stops. These dynamics result in the stage II melting as depicted in Fig. 3. To understand the melting dynamics in this stage, we plot the isotherms in the sample in which the phonon temperature T_p equals to 1234 K (the melting temperature T_m of Ag) and 1620 K as a function of time in Fig. 6. For regions in the sample for which $T_p > 1620$ K, we assume that they melt immediately because there is no energy barrier to melting. This treatment is consistent to the observations in MD simulations, which show that metals melt homogenously for $T_p > 1.2\ T_m$ (Ivanov et al., 2007; Delogu 2006). The actual position of the melt-front is therefore within the two isotherms. Note that the constant temperature contours can retract to the surface as the sample cools down, but the melting-front should only move forward and eventually stop when the temperature of the front is less than T_m. For reference, we include the experimentally measured velocity (≈ 350 m s^{-1}) as the dotted line in Fig. 6. The melting stops as the temperature of the front falls below T_m, which occurs at $t \approx$ 20-25 ps. This is consistent with the experiment in which the melting continues until t ≈ 30 ps.

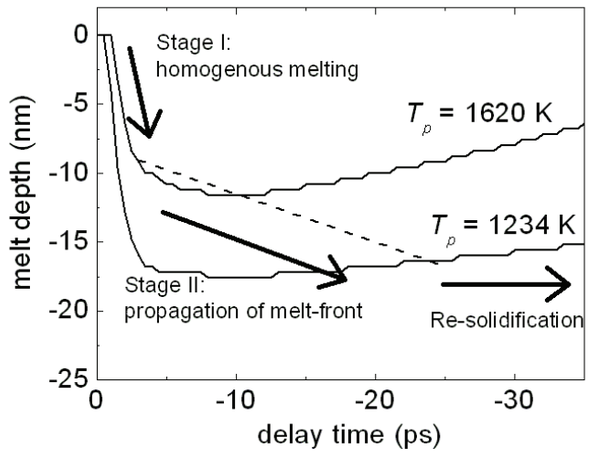

Fig. 6. Constant temperature contours at 1234 K and 1620 K calculated by TTM. In stage I melting, the solid melt homogenously along the T = 1620 K contour. In stage II, the melt-front propagates within these two contours. (Figure reprinted from Chan et al., 2008)

One of the interesting observations worth mention here is that during the stage II, when heat is transported away from a thin surface region (< 30 nm), a strong decoupling occurs between the phonon and electron system. This produces a situation characterized by 'hot' phonons and 'cold' electrons at the surface region, in contrast to 'hot' electrons and 'cold' phonons observed in stage I. To rationalize this interesting phenomenon, we note that heat is mainly carried away by the electrons. The heat from the hot phonons at the surface is first transferred to the electrons. Then, the heat is transported to the deeper regions by electrons. Hence, the rate of heat removal can be limited by the slow electron-phonon coupling of Ag. The decoupling can readily be observed from the results of the TTM. For example, in a 200 nm thick film, electron temperature T_e at the surface is just ≈ 100 K higher than T_e at back for t > 5 ps, regardless of the larger temperature difference (up to 1000K) in T_p. While different transport processes are included implicitly in the TTM, we can illustrate the phenomenon more clearly by calculating the effective conductance for heat carried away from a hot region of thickness h through electron G_{el} and phonon G_{ph}. The effective heat conductance for phonons, by dimensional analysis, is equal to κ_p / h (κ_p is phonon heat conductance). A thinner surface hot layer (i.e., smaller h) implies a steeper temperature gradient, which increases the effective heat conductance.

The conductance for electrons is more complicated. Heat must first be transferred from phonons in the hot surface layer to electrons, and it is carried away by electrons through diffusion. The transfer of heat back into the phonon system in the cold region is not the rate limiting process, assuming the cold reservoir is always much thicker than the hot region. The first step depends on the e-p coupling constant g and is proportional to the thickness of the hot layer. The conductance for this step is $G_{el\text{-}ep} = gh$. The conductance for the second step (electron diffusion) is $G_{el\text{-}d} = \kappa_{el}/h$. The conductance of electrons is the combination of the two conductances in series, which is given by

$$G_{el} = \frac{1}{\left(G_{el-ep}^{-1} + G_{el-d}^{-1}\right)} = \frac{1}{1/gh + h/\kappa_{el}}. \quad (4)$$

Normally $G_{el\text{-}ep} >> G_{el\text{-}d}$, which gives $G_{el} \approx G_{el\text{-}d}$. However, for small h and g, $G_{el\text{-}ep}$ can be small enough such that it will dominate the heat transport. In our case, taking h = 25 nm yields $G_{el\text{-}d} \approx 16$ GW m^{-2} K^{-1}, $G_{el\text{-}ep} \approx 0.9$ GWm^{-2}K^{-1}. It is thus clear that G_{el} is limited by e-p coupling and its value, calculated by Eq. (4) is 0.85 GW m^{-2} K^{-1}. In addition, this small value of G_{el} is the same order of magnitude as the phonon conductance G_{ph}. Using κ_p in our model, we find G_{ph} = 0.27 GW m^{-2} K^{-1}. Although G_{ph} is still smaller than G_{el}, it is no longer negligible as most studies have assumed. The phonon conduction, moreover, becomes increasingly more important as h falls below 25 nm.

The above behaviors should be general to other noble metals (Cu and Au) that have electronic structures similar to Ag. To summarize, the above analysis on Ag allows us to estimate the amount of materials that can be melted by fs-laser pulses before ablation occurs. This is important to applications such as micromachining where a precise control on the laser damaging depth is needed. For the group of noble metals discussed, the excitation of d-band electrons in stage I limits the depth of the initial heat deposition to approximately the optical absorption depth of the material. Subsequently, transport of heat by electrons from the excited region in stage II is limited by the weak e-p coupling. Although this limitation lengthens the melt lifetime, it is ineffective in increasing the total melt-depth, since most of the heat removed from the surface layer is evenly redistributed over the remainder of the film, i.e., a large temperature drops in the hot region is compensated by a small temperature rise in the cold region. Increasing the laser fluence does not increase the melt-depth appreciably since the extra energy results in ablation before the heat can spread into the bulk. For example, we have found that in our MD simulations, a Cu lattice becomes unstable at $T_p \approx 4000$ K (i.e. ablation will occur). Since the surface phonon temperature in our TTM calculation already reaches 2000 K and the heat confinement increases non-linearly as the laser fluence increases, we estimate that the maximum melt thickness is not larger than 30-40 nm before ablation becomes significant.

For comparison, we note that the above scenario can be much different if the effects of d-band excitation on thermal conductivity are not taken into account. The predicted melt-depth can be 3-5 times larger before the onset of ablation if the transport properties of noble metals at lower fluencies are used to model the melting dynamics.

4. Solidification of deeply-quenched melts

In the last part of this chapter, we will discuss the use of fs-laser pulses to study the ultrafast solidification dynamics of undercooled liquid Ag. This serves as an example in which we can use fs-lasers to produce a highly non-equilibrium phase. Furthermore, the time-resolved relaxation dynamics of the undercooled liquid can be studied quantitatively. Our experimental results do not agree with classical solidification theories (Chalmers, 1964), but are consistent with recent results from MD simulation. The MD simulation shows that a defect mechanism can describe the solidification behavior in a highly undercooled melt (Ashkenazy & Averback, 2007).

Quenching a pure metal into its glassy state has been a challenge to materials scientists over the last few decades (Turnbull & Cech, 1950). Two common ways to achieve this is either by removing the heterogeneous nucleation sites or by quenching the metals fast enough such that solidification does not have enough time to take place. Using traditional techniques, a pure metal can at most be quenched to $\approx 0.8\ T_m$ because of its extremely fast solidification kinetics. Ultrafast lasers provide a new way to achieve this goal because it can confine the

melt in a very few surface region (10s of nm) while keeping the remainders of the sample cold. As we will see below, quenching rates as fast as 5×10^{12} K s^{-1} can be achieved.
There have been some earlier attempts to use ps or ns lasers to undercool liquids. However, in the ps-laser studies (MacDonald et al., 1989; Agranat et al., 1999), only resolidification time can be measured quantitatively. Important parameters such as surface temperature and solidification velocity remain unknown. In the ns-laser studies, the pulses are too long and a thick layer of materials can be heated up within the pulse duration. Hence, no significant undercooling can be achieved (Tsao et al., 1986; Smith & Aziz, 1994). In our current experiment with fs-lasers, we are able to quench the liquid with large undercooling and measure the solidification velocity quantitatively using the optical TH generation described above. The undercooling temperature is modeled by TTM with a high accuracy. As a result, we can measure the solidification velocity as a function of temperature down to ≈ 0.6 T_m.

4.1 Ultrafast quenching and solidification of undercooled liquid

Single crystals Ag grown on MgO substrates were used in the experiment. The details of the experiments can be found in (Chan et al., 2009b). A schematics diagram for the experiment is shown in Fig. 7. A thin layer of Ag is melted by the fs-laser pulse. The optical TH generation technique discussed in Sec. 3.1 was used to measure the position of the crystal-melt interface as a function of time. The rate of resolidification depends on the undercooling of the liquid Ag. The degree of undercooling during solidification can be readily controlled by simply changing the thickness of the thin films, which will be discussed below.

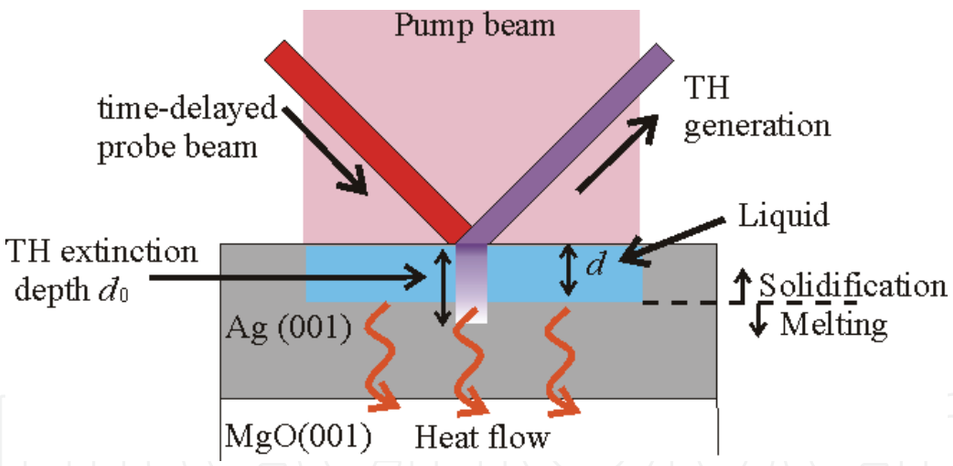

Fig. 7. A schematic of the experiment setup. The pump beam, which is ≈ 10 times larger in size than the probe beam, is used to melt the Ag. Optical TH generation is used to measure the thickness d of the liquid layer. The cooling rate is controlled by varying the thickness of the Ag layer. (Figure reprinted from Chan et al., 2009b)

Figure 8 shows the results for three Ag films with different film thicknesses. After the initial melting, the TH intensity recovers steadily for t > 50 ps, which represents resolidification of the liquid phase. The slope of the solid line represents the average interfacial velocity v_{ave}. The solidification process is completed by t ≈ 200 - 300 ps. The signal does not fully recover at t ≈ 1 ns, but it does so, however, before t ≈ 1 s. We attribute the degradation in signal at t = 1 ns to the production of quenched-in defects (primarily vacancies) during solidification, such defects have been observed in MD simulations (Lin et al., 2008a).

Note that the solidification velocity varies with the film thicknesses. The conductance of heat through the thin Ag film is much faster than through the Ag-MgO interface and the MgO substrate. During the solidification, therefore, the heat spreads rapidly across the entire Ag film, but only a small amount of heat can transport across the Ag-MgO interface. Larger undercoolings (or low temperatures) are thus achieved in thicker films.

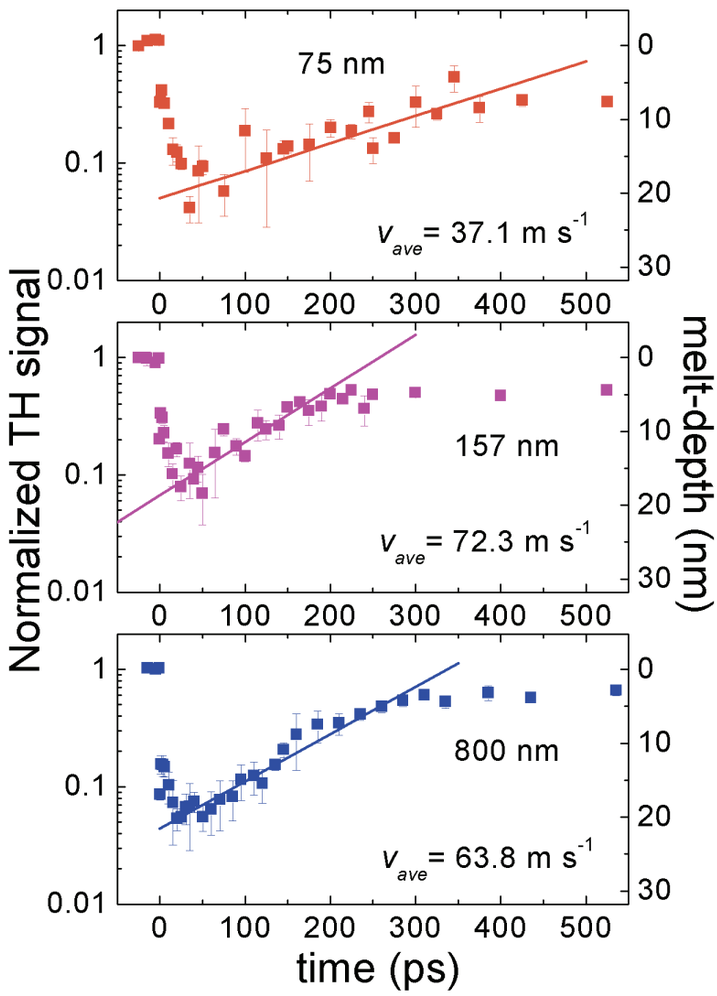

Fig. 8. The TH signal as a function of time measured for samples with three different thicknesses of the Ag layer. The converted melt-depth is shown on the axis on the right. The average resolidification velocity is indicated by the solid-lines. (Figure reprinted from Chan et al., 2009b)

We determine the temperature of the crystal-melt interface using TTM. For the solidification process, since the electronic system has already restored the Fermi-Dirac distribution, the TTM model is aimed at determining the interface temperatures with high accuracy. The details of the model can be found in (Chan et al., 2009b). Here, we note that the parameter in the model that has the strongest effect on the calculated temperatures is the total energy initially absorbed by the samples. Instead of modeling this parameter, we have measured it directly using the calorimetry setup discussed in Sec. 2. Figure 9 shows the interface

temperature as a function of time for different film thicknesses. By combining the average temperature determined from the TTM and the v_{ave} found in experiment, we can plot the solidification velocity as a function of temperature, which is shown in Fig. 10.

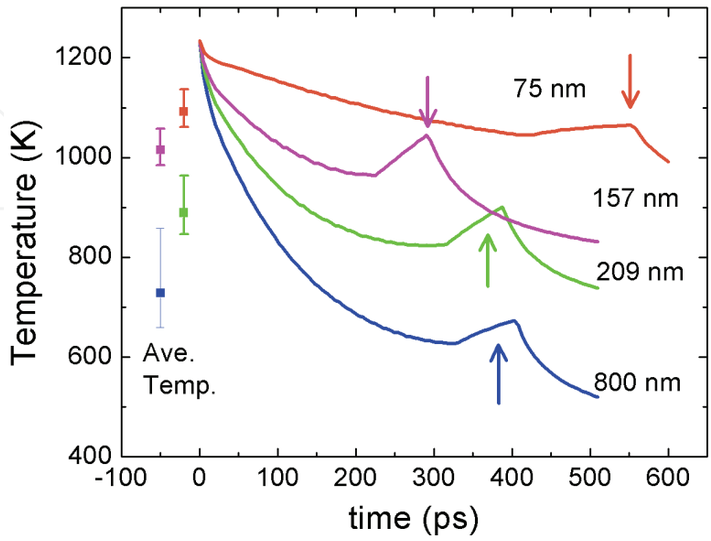

Fig. 9. The interface temperature as a function of time. The arrows indicate the end of the solidification. The average temperatures over the whole period of solidification are indicated by the solid-symbols on the left. The error bars above (below) the symbols represent the mean deviations from the average temperature during the period with temperatures above (below) the average temperature. (Figure reprinted from Chan et al., 2009b)

The solidification velocity is also obtained as a function of temperature using MD simulation (Ashkenazy & Averback 2007; 2010); these data are shown in Fig. 9 as circles. The agreement between experiment and simulation is quite good; note that there are no adjustable parameters. The velocity increases approximately linearly from T_m to 0.85 T_m, and then it becomes insensitive to temperature with further decrease in temperature. The long plateau observed in Fig. 10 explains why the experimental solidification velocity remains nearly constant as a function of time even though Fig. 9 shows that the crystal-melt interface temperature can vary by ≈ 200 – 300 K during solidification.

4.2 Kinetics mechanisms for solidification

Although continuum models for solidification have been developed for decades, none of these models have been experimentally verified in a pure metal at deep undercooling. This is mainly due to the difficulty in quenching a pure metallic liquid far below its melting point. The classical model assumes that the solidification rate in pure is controlled by collision-limited kinetics (MacDonald et al., 1989; Coriell & Turnbull, 1983; Broughton et al., 1982). Furthermore, it is often accepted that there is no energy barrier for an atom to move across the liquid-solid interface. Under these assumptions, the velocity can be written as

$$v(T) = C\sqrt{\frac{3kT}{m}}\left[1 - \exp\left(-\Delta\mu/kT\right)\right], \tag{5}$$

where C is a geometric factor on the order of 1, m is the atomic mass and $\Delta\mu$ is the free energy difference between the solid and liquid phase. This relation is shown as the solid line in Fig. 9. Because of the weak $(T)^{1/2}$ dependence, the velocity continues to increase until $T < 0.3\ T_m$; this clearly disagrees with the experimental and simulation data shown in Fig. 10.

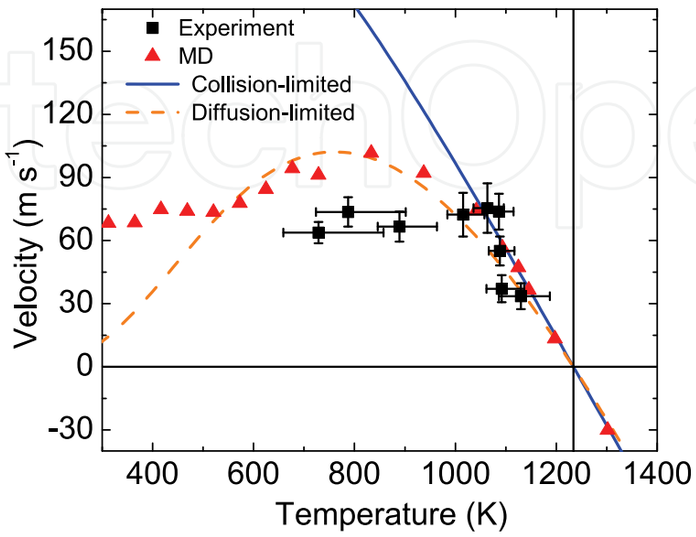

Fig. 10. Solidification velocities verse the temperatures. The experimental data (squares) show reasonable agreement to the MD simulations (triangles). However, it clearly deviates from the collision-limited model (the blue solid line). If we assume the motion of the atom across the liquid-solid interface is thermally activated (with an activation barrier = 0.12 eV), the predicted velocity is shown as the orange line (dashed-line). (Figure reprinted from Chan et al., 2009b)

If a barrier exists in the energy landscape for an atom to move from the liquid to the solid, one can replace the square root term in Eq. (5) by an exponential term $A\exp(-E/kT)$ (Frenkel, 1946), where E represents the barrier height. By setting E = 0.12eV and A = 1300 m s^{-1}, indicated by the orange (dashed) line in Fig. 10, we see that above 600 K, the velocity agrees well with the MD simulation and the experimental data. The existence of an activation barrier, therefore, can explain why the solidification velocity reaches its maximum at a relatively high temperature. Such a barrier, however, indicates that the velocity should diminish at lower temperatures, which disagrees with the MD simulations. We note that in Ag the glass transition temperature $T_g \approx 600$K. The discrepancy between the continuum models and the MD data perhaps suggests that the solidification mechanisms for the liquid and glass states may be very different.

Our recent MD simulation (Chan et al., 2010) shows that atoms at the interface transform into the crystalline phase cooperatively instead of individually as assumed in the classical models. In our simulations, the transformation is often induced by 1 or 2 atoms making exceptional long jumps, the nearest neighbors surrounding these atoms then transform into the crystalline phase cooperatively. Interestingly, the magnitude and directionality of these long jumps is very similar to the motion of an interstitial defect in the crystalline phase. These observations agree with the model proposed earlier by Ashkenazy and Averback (Ashkenazy & Averback, 2007), in which the solidification kinetics is controlled by interstitial-like motions at the crystal-melt interface. To prove this model experimentally, we

need to quench the liquid below its glass transition temperature. Currently, we are not able to achieve these deep undercoolings, but with more carefully designed experimental systems, more tunable laser systems, or advance characterization techniques such as time-resolved diffraction, this goal appears within reach.

5. Conclusion

In this chapter, we have presented a comprehensive study on the heat absorption, transport, and phase transformation kinetics in Ag irradiated by fs-lasers. Although the current study is focused on Ag, but similar behaviors are expected to be observed in Cu and Au as well. We have shown that a lot of complexities on the optical and transport properties can arise at fluences close to the melting and ablation threshold. These complexities come from the excitation of electron bands that are below the Fermi level. Although noble metals are among the most-studied materials, at these high excitations, many fundamental issues such as the relaxation of non-equilibrium hot electrons, the thermal transport under extremely high temperature gradients, and the dynamics of superheated solid are still not well-resolved. We can expect similar complex situations can be found in other transition metals as well.

We also demonstrated that by the using of fs-lasers, we can induce ultrafast quenching in Ag and measure the transformation kinetics of the undercooled liquid quantitatively. This only serves as one of the examples in which we can use fs-laser to drive materials into structurally unstable phases. With the rapid development of the laser technologies and time-resolved characterization techniques, we can study phases that are inaccessible before. This not only improves our understanding of materials under extreme environments, but also provides us new ways to create metastable materials that have novel structural and electronic properties.

6. Acknowledgement

We gratefully acknowledge the supports by the U.S. Department of Energy - NNSA under Grant No. DE-FG52-06NA26153 and the U.S. Department of Energy-BES under Grants No. DE-FG02-05ER46217.

7. References

Agranat, M. B.; Ashitkov, S. I.; Fortov, V. E.; Kirillin, A. V.; Kostanovskii, A. V.; Anisimov, S. I. & Kondratenko, P. S. (1999). Use of optical anisotropy for study of ultrafast phase transformations at solid surfaces. *Appl. Phys. A*, 69, 6, 637-640 , ISSN: 0947-8396

Anisimov, S. I.; Kapeliovich, B. L. & Perel'man, T. L. (1974). Electron emission from metal surfaces exposed to ultrashort laser pulses. *Sov. Phys. JETP*, 39, 375-377, ISSN: 1063-7761

Ashkenazy, Y. & Averback, R. S. (2010). Kinetic stages in the crystallization of deeply undercooled body-centered-cubic and face-centered cubic metals. *Acta Materialia*, 58, 2, 524-530, ISSN: 1359-6454

Ashkenazy, Y. & Averback, R. S. (2007). Atomic mechanisms controlling crystallization behavior in metals at deep undercoolings. *EPL*, 79, 2, 26005, ISSN: 0295-5075

Baber, W. G. (1937). The Contribution to the Electrical Resistance of Metals from Collisions between Electrons. *Proc. Roy. Soc. A* , 158, 383-396, ISSN 1364-5021

Bonn, M.; Denzler, D. N.; Funk, S. ; Wolf, M. ; Svante Wellershoff, S. & Hohlfeld, J. (2000). Ultrafast electron dynamics at metal surfaces: Competition between electron-phonon coupling and hot-electron transport. *Phys. Rev. B*, 61, 2, 1101-1105, ISSN 1098-0121

Broughton, J. Q.; Gilmer, G. H. & Jackson, K. A. (1982). Crystallization Rates of a Lennard-Jones Liquid. *Phys. Rev. Lett.*, 49, 20, 1496-1500, ISSN 0031-9007

Butcher, P. N. & Cotter D. (1990). *The Elements of Nonlinear Optics*, Cambridge University Press, ISBN: 0-521-34183-3, Cambridge

Cerchez, M.; Jung, R.; Osterholz, J.; Toncian, T.; Willi, O.; Mulser, R. & Ruhl, H. (2008). Absorption of Ultrashort Laser Pulses in Strongly Overdense Targets. *Phys. Rev. Lett.*, 100, 24, 245001, ISSN 0031-9007

Chalmers, B. (1964). *Principles of solidification*, John Wiley & Son, ISBN: 0471143251, New York

Chan, W. –L.; Averback, R. S. & Ashkenazy, Y. (2010). Anisotropic atomic motion at undercooled crystal/melt interfaces. *Phy. Rev. B*, 82, 2, 020201(R), ISSN 1098-0121

Chan, W. L.; Averback, R. S. & Cahill, D. G. (2009a). Nonlinear energy absorption of femtosecond laser pulses in noble metals. *Appl. Phys. A*, 97, 2, 287-294, ISSN: 0947-8396

Chan, W. -L.; Averback, R. S.; Cahill, D. G. & Ashkenazy, Y. (2009b). Solidification Velocities in Deeply Undercooled Silver. *Phys. Rev. Lett.*, 102, 9, 095701, ISSN 0031-9007

Chan, W.-L.; Averback, R. S.; Cahill, D. G. & Lagoutchev A. (2008). Dynamics of femtosecond laser-induced melting of silver. *Phys. Rev. B*, 78, 21, 214107, ISSN 1098-0121

Coles, B. R. & Taylor, J. C. (1962). The Electrical Resistivities of the Palladium-Silver Alloys. *Proc. Roy. Soc. A*, 267, 139-145, ISSN 1364-5021

Coriell, S. R. & Turnbull, D. (1982). Relative roles of heat transport and interface rearrangement rates in the rapid growth of crystals in undercooled melts. *Acta. Metall.*, 30, 12, 2135-2139, (1982), ISSN: 0001-6160

Delogu, F. (2006). Homogeneous melting of metals with different crystalline structure. *J. Phys.: Condens. Matter*, 18, 24, 5639-5654, ISSN: 0953-8984

Eesley, G. L. (1983). Observation of Nonequilibrium Electron Heating in Copper. *Phys. Rev. Lett.*, 51, 23, 2140-2143, ISSN 0031-9007

Ernstorfer, R.; Harb, M.; Dartigalongue, T.; Hebeisen, C. T.; Jordan, R. E.; Zhu, L. & Miller, R. J. D. (2007). Femtosecond Electron Diffraction Study on the Melting Dynamics of Gold, In: *Springer Series in Chemical Physics Vol. 88: Ultrafast Phenomena XV*, Corkum, P.; Dwayne Miller, R. J.; Jones, D. M. & Weiner, A. M. (Ed.), 755-757, Springer, ISBN: 978-3-540-68779-5, Berlin

Fuster, G.; Tyler, J. M.; Brener, N. E.; Callaway, J. & Bagayoko, D. (1990). Electronic structure and related properties of silver. *Phys. Rev. B*, 42, 12, 7322-7329, ISSN 1098-0121

Frenkel, J. (1946). *Kinetic Theory of Liquids*, Oxford University Press, Oxford

Gattass, R. R. & Mazur E. (2008). Femtosecond laser micromachining in transparent materials. *Nature photonics*, 2, 4, 219-225, ISSN 1749-4885

Gundrum, B. C.; Cahill, D. G. & Averback, R. S. (2005). Thermal conductance of metal-metal interfaces. *Phys. Rev. B*, 72, 24, 245426, ISSN 1098-0121

Ivanov, D. S. & Zhigilei, L. V. (2007). Kinetic Limit of Heterogeneous Melting in Metals. *Phys. Rev. Lett.*, 98, 19, 195701, ISSN 0031-9007

Kittle, C. (2005). *Introduction to Solid States Physics – 8th ed.,* John Wiley & Son, ISBN: 0-471-41526-X, New York

Lin, Z.; Johnson, R. A. & Zhigilei, L. V. (2008a). Computational study of the generation of crystal defects in a bcc metal target irradiated by short laser pulses. *Phys. Rev. B*, 77, 21, 214108, ISSN 1098-0121

Lin, Z.; Zhigilei, L. V. & Celli, V. (2008b). Electron-phonon coupling and electron heat capacity of metals under conditions of strong electron-phonon nonequilibrium. *Phys. Rev. B*, 77, 7, 075133, ISSN 1098-0121

Liu, X.; Du, D. & Mourou, G. (1997). Laser ablation and micromachining with ultrashort laser pulses. *IEEE J. Quantum Electronics*, 33, 10, 1706-1716, ISSN 0018-9197

MacDonald, A. H. & Geldart, D. J. W. (1980). Electron-electron scattering and the thermal resistivity of simple metals. *J. Phys. F: Metal Phys.*, 10, 4, 677-692, ISSN: 0305-4608

MacDonald, C. A.; Malvezzi, A. M. & Spaepen, F. (1988). Picosecond time - resolved measurements of crystallization in noble metals. *J. Appl. Phys.*, 65, 1, 129-136, ISSN 0021-8979

Mahan, G. D. & Claro, F. (1988). Nonlocal theory of thermal conductivity. *Phys. Rev. B*, 38, 3, 1963-1969, ISSN 1098-0121

Milchberg, H. M.; Freeman, R. R.; Davey, S. C. & More, R. M. (1988). Resistivity of a Simple Metal from Room Temperature to 10^6 K. *Phys. Rev. Lett.*, 61, 20, 2364-2367, ISSN 0031-9007

Miller, J. C. (1969). Optical properties of liquid metals at high temperatures. *Phil. Mag.*, 20, 168, 1115-1132, ISSN: 1478-6435

Miyaji, G. & Miyazaki K. (2008). Origin of periodicity in nanostructuring on thin film surfaces ablated with femtosecond laser pulses. *Optics express*, 16, 20, 16265-16271, ISSN 1094-4087

Mott, N. F. (1936). The Electrical Conductivity of Transition Metals. *Proc. Roy. Soc. A*, 153, 699-717, ISSN 1364-5021

Norris, P. M.; Caffrey, A. P.; Stevens, R. J.; Klopf, J. M.; McLeskey Jr., J. T. & Smith, A. N. (2003). Femtosecond pump–probe nondestructive examination of materials (invited). *Rev. Sci. Instrum.*, 74, 400-406, ISSN 0034-6748

Perry, M. D.; Stuart, B. C.; Banks, P. S.; Feit, M. D.; Yanovsky, V. & Rubenchik, A. M. (1999). Ultrashort-pulse laser machining of dielectric materials. *J. Appl. Phys.*, 85, 9, 6803-6810, ISSN 0021-8979

Pines, D. (1999). *Elementary excitations in solids*, Perseus Books, ISBN: 0738201154, Massachusetts

Smith, P. M. & Aziz, M. J. (1994). Solute trapping in aluminum alloys. *Acta. Metall. Mater.*, 42, 10, 3515-3525, ISSN: 0956-7151

Suarez, C.; Bron, W. E. & Juhasz, T. (1995). Dynamics and Transport of Electronic Carriers in Thin Gold Films. *Phys. Rev. Lett.*, 75, 24, 4536-4539, ISSN 0031-9007

Tas, G. & Maris, H. J. (1994). Electron diffusion in metals studied by picosecond ultrasonics. *Phys. Rev. B*, 49, 21, 15046-15054, ISSN 1098-0121

Tsao, J. Y.; Aziz, M. J.; Thompson, M. O. & Peercy, P. S. (1986). Asymmetric Melting and Freezing Kinetics in Silicon. *Phys. Rev. Lett.*, 56, 25, 2712-2715, ISSN 0031-9007

Turnbull, D. & Cech, R. E. (1950). Microscopic Observation of the Solidification of Small Metal Droplets. *J. Appl. Phys.*, 21, 8, 804-810, ISSN 0021-8979

Vorobyev, A. Y. & Guo, C. (2004). Direct observation of enhanced residual thermal energy coupling to solids in femtosecond laser ablation. *Appl. Phys. Lett.*, 86, 1, 011916, ISSN 0003-6951

Vorobyev, A. Y. & Guo, C. (2008). Colorizing metals with femtosecond laser pulses. *Appl. Phys. Lett.*, 92, 4, 041914, ISSN 0003-6951

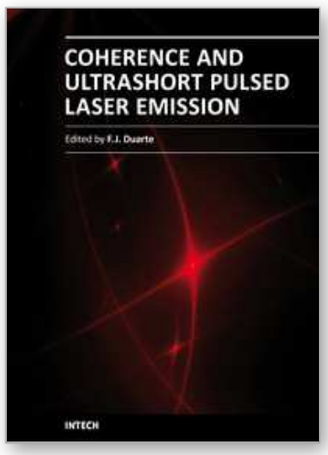

Coherence and Ultrashort Pulse Laser Emission

Edited by Dr. F. J. Duarte

ISBN 978-953-307-242-5
Hard cover, 688 pages
Publisher InTech
Published online 30, November, 2010
Published in print edition November, 2010

In this volume, recent contributions on coherence provide a useful perspective on the diversity of various coherent sources of emission and coherent related phenomena of current interest. These papers provide a preamble for a larger collection of contributions on ultrashort pulse laser generation and ultrashort pulse laser phenomena. Papers on ultrashort pulse phenomena include works on few cycle pulses, high-power generation, propagation in various media, to various applications of current interest. Undoubtedly, Coherence and Ultrashort Pulse Emission offers a rich and practical perspective on this rapidly evolving field.

InTech Europe
University Campus STeP Ri
Slavka Krautzeka 83/A
51000 Rijeka, Croatia
Phone: +385 (51) 770 447
Fax: +385 (51) 686 166
www.intechopen.com

InTech China
Unit 405, Office Block, Hotel Equatorial Shanghai
No.65, Yan An Road (West), Shanghai, 200040, China
中国上海市延安西路65号上海国际贵都大饭店办公楼405单元
Phone: +86-21-62489820
Fax: +86-21-62489821

IntechOpen